Draft version November 3, 2026
Typeset using LaTeX **default** style in AASTeX7.0.1

# The ExtraSolar Coronagraph for the Lazuli Space Observatory: Design

Ewan Douglas [1], Simran Agarwal [2], Ramya Anche [2], Cameron Ard [2], Solvay Blomquist [2], Steven Burrows [2], Heejoo Choi [2], Fernando Coronado [2], Katie A. Crotts [2], Kevin Derby [2], Olivier Durney [2], Jess Andrew Johnson [2], Hyukmo Kang [2], Nicholas Lambert [2], Hiram Olivas [2], Summer Franks [2], Mike Eiklenborg [2], Nick Emerson [2], Aaron Granados [2], Elizabeth Fucetola [2], Cat Hathaway [2], Sebastiaan Y. Haffert [3], Christian Haughwout [4], Justin Hom [2], Ruby Huie [2], Patrick Ingraham [2], Sarah Kay [2], Stephen Kaye [2], Michael Otto Koehler [2], Douglas Kelly [2], Maggie Y Kautz [2], Daewook Kim [2], Jay Kueny [2], Yu-Chia Lin [2], Jared R. Males [2], Kian Milani [2], Christopher Mendillo [5], Steve Meyer [2], Kelsey Lynn Miller [2], Jane Morrison [2], Oscar Montoya [2], Pierre Nicolas [2], Laurent Pueyo [6], Sai Krishanth Pulikesi Mannan [2], Carson Quimby [2], Stephanie Rinaldi [2], Trupti Ranka [2], Joanna Rosenbluth [2], Adam Schilperoort [2], Nicholas Thomas Schragal [2], Irina Stefan [2], Robert Stone [2], Saraswathi Kalyani Subramanian [2], Kyle Van Gorkom [2], Grant West [2], Andre F. Wong [2], and Jaegun Yoo [2]

[1] *Steward Observatory, University of Arizona, 933N Cherry Avenue, Tucson, Arizona, 85721, USA*
[2] *University of Arizona, Tucson, AZ 85721, USA*
[3] *Leiden*
[4]
[5] *UML*
[6] *STScI*

Draft

## ABSTRACT

Imaging reflected light from planets in other star systems will open the door to a better understanding of the processes that drive planet formation, atmospheric properties, and the conditions that lead to life. Around mature Sun-like stars, reflected light from planets and debris disks in the liquid water habitable zone are expected to be approximately 10 ppb or dimmer, whereas current observatories are sensitive to thermal emission from giant planets and collisionally dominated disks. Recent technological breakthroughs have brought ultra-high-contrast imaging of reflected light into reach for space-based telescopes. A 3 m class coronagraphic telescope can achieve $10^{-8}$ or better planet-star flux ratio sensitivity. We describe the ExtraSolar Coronagraph (ESC) instrument concept for the Lazuli Space Observatory, part of the Eric and Wendy Schmidt Observatory System. The two-channel, vector vortex coronagraph is designed to a requirement of $< 10^{-7}$ raw normalized intensity on sky at 630 nm, with a design goal of $10^{-8}$, and final post-processed performance is expected to greatly exceed that. The design is informed by laboratory experiments on the University of Arizona Space Coronagraph Optical Bench testbed which has achieved $9 \times 10^{-9}$ contrast on a zeroth-magnitude source in the lab and $4 \times 10^{-9}$ in 2% bandwidth on a bright supercontinuum laser source. The ESC design opens a range of new science cases including imaging of giant exoplanets, exo-asteroid belts, and exozodiacal dust in reflected light.

Contents

1. Introduction 3

2. System requirements and design methodology 3

3. Instrument design 3
3.1. Heritage and risk approach 4
3.2. Control loops and block diagram 8
3.2.1. Wavefront control 8
3.3. Dichroic beamsplitter 9
3.4. Fine pointing 9
3.5. Polarization filtering 9
3.6. Deformable mirrors 10
3.7. Vector vortex waveplate 11
3.8. Filter selection 11
3.9. Sensors 11
3.10. Compute and software platform 13
3.11. High-order wavefront sensing approach 13
3.12. Low-order wavefront sensing approach 13

4. Optical design and analysis 14

5. Diffraction model: sensitivity analysis and instrument performance 14
5.0.1. LLOWFS residuals and DZM 14

6. Contrast budget 14

7. Concept of science operations and expected science performance 14
7.1. Concept of operations 14
7.2. Calibration 15
7.3. Brief overview of potential science cases 16
7.3.1. Exoplanets 16
7.3.2. Circumstellar dust 16
7.3.3. Surveying our nearest stellar neighbors 16

8. Current performance in the lab using VVC 17
8.1. Low-flux dark zone 17
8.2. Demonstration of LLOWFS 17

9. Software 17
9.1. Flight Software 17
9.2. Simulation 17
9.3. Systems Engineering 17

10. Summary and discussions 17

11. Software and third-party data repository citations 17

A. Post-processing factor and contrast budget terms 18

Draft

## 1. INTRODUCTION

Our understanding of the processes that regulate planet formation and the architecture of stellar systems has been significantly advanced by high-resolution astronomy.

Our knowledge of the conditions under which solar-system-like planets form has advanced with recent advances in high-contrast imaging which has enabled direct imaging of young exoplanets and both protoplanetary and evolved circumstellar disks (see reviews by B. P. Bowler 2016; L. Pueyo 2018; A. M. Hughes et al. 2018; A. Zurlo 2026). However, our understanding of mature systems with tenuous solar-system analog debris disks and planets visible only in reflected light is lacking. Since the star-planet reflected light flux ratio depends on planet reflecting area and distance from the star, contrasts for planets of equal masses vary widely; for example, for a Neptune-size planet the flux ratio at 0.8 au is $5 \times 10^{-9}$ vs. $3 \times 10^{-11}$ at 10 au. Adding atmospheric quantities like condensing species and absorption complicates the picture and requires extensive modeling.

This paper introduces the ExtraSolar Coronagraph (ESC), a space coronagraph designed to image exoplanets and debris disks in scattered light. Numerous techniques have been developed to attenuate or subtract starlight relying on the instrument maintaining a stable or predictable influence on the phase and amplitude of that light. From space, wavefront errors are all internal, both thermal and manufacturing and alignment errors. The ESC uses active wavefront control to reach a raw-contrast design goal of $\sim 10^{-8}$ and post-processing to reach sensitivities $\sim 10^{-9}$.

## 2. SYSTEM REQUIREMENTS AND DESIGN METHODOLOGY

## 3. INSTRUMENT DESIGN

Space coronagraph design is an iterative process of maximizing sensitivity to planets of interest while minimizing telescope and instrument complexity. Our approach was first to select a mature starlight suppression technology which placed minimal requirements on the observatory and then refine the remaining requirements on an observatory to maintain an astrophysically relevant contrast floor via a robust contrast budget which was toleranced via realistic end-to-end control system simulations and anchored by laboratory tests. Performance estimates in this paper are for the red arm; the blue-arm contrast budget and throughput are future work. Table 1 summarizes the key instrument parameters.

Draft

w of the Lazuli ESC instrument concept: current best estimates. Angular scales assume the 3 m Lazuli aperture (A. Roy et al. 2026); the inner and o
t 3 and 10 $\lambda/D$ used in the contrast budget.

| | Blue arm | Red arm |
|---|---|---|
| Focal Plane mask | Charge-6 LCP VVW | |
| Wavelength bands ($\mu$m) | 0.40–0.475 | 0.62–0.757 |
| VVW center wavelength | 440 nm | 630 nm |
| VVW bandwidth (20% of center) | 396–484 nm | 567–693 nm |
| Pixel size (5 pixels per $\lambda/D$) | $\leq$6.2 mas (at 450 nm) | $\leq$8.5 mas (at 620 nm) |
| Telescope resolution ($\lambda/D$ at VVW center) | 30 mas | 43 mas |
| IWA (3 $\lambda/D$) | 91 mas | 130 mas |
| OWA (10 $\lambda/D$) | 0.3 arcsec | 0.4 arcsec |
| FOV full-width | $> 5''$ | $> 5''$ |
| Raw contrast (CBE) | $< 10^{-8}$ | |
| Post-processed contrast (anticipated) | $10^{-9}$ | |
| On-sky polarization | fixed single linear state (polarizer + QWP) | |
| Wavefront control | single MEMS DM, iEFC, one-sided dark zone, Lyot-based LOWFS, fast steering mirror | |
| Deformable mirror | BMC Kilo-C-1.5 | BMC 2K |
| | $34 \times 34$ (952 active), 30 illuminated | $50 \times 50$ (2040 active), 45 illuminated |
| | 300 $\mu$m pitch | 400 $\mu$m pitch |
| Detector | CMOS | |
| Lyot-stop diameter | 0.9D | |

NOTE—Final contrast values depend on telescope parameters (wavefront stability, pointing jitter, and polarization aberrations) that are outside the scope of this work. Performance estimates in this paper are for the red arm.

Draft

### 3.1. *Heritage and risk approach*

The short schedule of the Lazuli program (A. Roy et al. 2026) dictates minimum technology development and maximization of commercial off-the-shelf (COTS) hardware. An off-the-shelf approach minimizes schedule risk but introduces performance risks if COTS hardware, when tested, does not perform as expected. We thus have attempted to constrain the coronagraph design to previously laboratory demonstrated technologies where the engineering challenges of adaptation fit within the program schedule. A few notable exceptions, such as sensors and dichroic beamsplitters are noted below. Within the available options, priority was given to low-Size, Weight, and Power (SWaP) technologies that are readily commercially available.

Construction of the University of Arizona Space Coronagraph Optical Bench (SCoOB) testbed was initiated in 2020 as a platform for raising the technology readiness level of integrated coronagraphic systems (E. R. Maier et al. 2020; J. N. Ashcraft et al. 2022, 2024; R. M. Anche et al. 2024, 2025), and has demonstrated high-and low-order wavefront control (K. Van Gorkom et al. 2022; K. Derby et al. 2025) of various coronagraph designs (K. Van Gorkom et al. 2024; K. Milani et al. 2025). Broadband absolute contrast on SCoOB is currently expected to be limited by chromatic aberrations (K. Van Gorkom et al. 2026).

The SCoOB testbed design and implementation draws on decades of worldwide work to develop exoplanet coronagraphy that is too extensive to completely summarize here. Some particularly impactful work includes mission concepts such as HabEx (B. Mennesson et al. 2016; B. S. Gaudi et al. 2020), LUVOIR (T. L. Team 2019), WFIRST-AFTA (N. J. Kasdin & et al. 2020), ACESat (E. A. Bendek et al. 2015), EXCEDE (R. Belikov et al. 2014; O. Guyon et al. 2012); testing of Vector Vortex Coronagraph (VVC) at JPL (D. Mawet et al. 2009; **?**; G. Serabyn et al. 2019; G. Ruane et al. 2022; J. Llop-Sayson et al. 2024). Testing of MEMS deformable mirrors in the lab (K. M. Morzinski et al. 2012;

C. M. Prada et al. 2021) and in space (C. B. Mendillo et al. 2012b; E. S. Douglas et al. 2018; S. K. Vlahakis 2022), Lyot low-order wavefront sensor (LLOWFS) on the ground and on balloons (**?**C. B. Mendillo et al. 2023), implicit electric-field conjugation (iEFC) image plane wavefront sensing algorithm development and test (**?**S. F. Redmond et al. 2022a; S. Y. Haffert et al. 2023) and self-coherent camera (SCC) on THD2 (A. Potier et al. 2020). Table 2 summarizes the key ESC technologies and their flight, suborbital, ground-based, and laboratory heritage.

Draft

**Table 2**. Key ESC technologies and their heritage. Ground-based and laboratory programs are credited as heritage alongside orbital and suborbital flight.

| Element | ESC baseline | Flight / suborbital heritage | Ground / laboratory heritage | Demonstrated performance |
|---|---|---|---|---|
| Focal-plane mask | Charge-6 LCP vector vortex | PICTURE-C balloon (1, 2, 3) | JPL HCIT TDEM (4, 5); HCIT vacuum tests (6); SCoOB (7); on-sky VVC at Palomar (8, 9); $\gamma$ irradiation of LCP devices (10) | $1.3 \times 10^{-8}$ at 575 nm, 10% BW (5); $\lesssim 10^{-8}$ on SCoOB (7) |
| Red-arm DM | BMC 2K MEMS, 2040 actuators | MEMS DM Kilo on PICTURE-B (11); Mini on DeMi CubeSat (12) | Carrier vibration-tested and demonstrated at HCIT (13); 2K on sky in MagAO-X (14, 15) and SCExAO (16); 4K on sky in GPI (17, 18) | $10^{-8}$-class dark zones (HCIT); years of on-sky operation (15) |
| Fine steering mirror | PI S-316 piezo stage, 500 Hz | Same stage on PICTURE and PICTURE-B, 5 mas (19) | - | 5 mas on 0.5 m suborbital telescope (19) |
| Low-order WFS/C | Lyot-reflected defocused LLOWFS, 10 Zernikes, FSM/DM offload | PICTURE-C (3, 20) | On-sky VVC+LLOWFS at SCExAO (21, 22); SCoOB with concurrent iEFC (23, 24) | $10^{-8}$ held for 2 h on SCoOB (24) |
| High-order WFS | iEFC baseline, EFC fallback, single DM | EFC baselined on Roman CGI (25, 26) | iEFC algorithm and MagAO-X bench (27, 28); robustness simulations (29); SCoOB (24); EFC (30, 31); on-sky iEFC at MagAO-X (32); on-sky EFC at VLT/SPHERE (33) | $9.5 \times 10^{-9}$ on 0-mag source; $4 \times 10^{-9}$ at 2% BW (34) |
| Dark-zone maintenance | Modal EKF DZM, LDFC, optional SCC | None (Roman CGI set-and-forget) | SCoOB (35, 36); HCIT DZM (37, 38); LDFC (39); dither DZM (40); on-sky LDFC at SCExAO (41); SCC at THD2 (42); on-sky SCC at Palomar (43) | $10^{-8}$ with MEMS DM at THD2 (42) |
| Polarization filtering | Polarizer + QWP pairs around VVC | Roman CGI polarizer optics (44); PICTURE-C (2) | HCIT VVC tests (5); design basis (45); SCoOB Mueller-matrix characterization (46) | Budgeted leakage $1.5 \times 10^{-10}$ |
| Dichroic beamsplitter | Custom WFE-optimized red/blue split | None upstream of a $10^{-8}$ coronagraph | Design and modeling (47); dichroic coronagraphic performance on a testbed (48); dichroic-fed arms on SPHERE (49) and MagAO-X (14) | Modeled and bench-tested |
| Detectors | Low-noise CMOS (HWK4123, IMX492 candidates) | - | SCoOB end-to-end without field stop (7); sensor characterization (50); pre-irradiation characterization of the HWK4123 and radiation test plan (51); HWK4123 proton irradiation at TRIUMF, TID and single-event response (52) | $0.5\,e^-$ read noise (50) |
| Compute and software | CACAO + MagAO-X XWCTk, Linux, GPU | Neutralino ISS Surveyor | On sky at Subaru/SCExAO and Magellan/MagAO-X (53, 54, 55); runs SCoOB (56) | kHz AO loops on 6.5–8 m telescopes (15) |
| Filter wheel | Eight-position wheel per arm holding the science filters, pupil-imaging lens, and dark block (Table 3) | OSIRIS-REx OCAMS MapCam eight-position filter wheel, built at the University of Arizona operated throughout the Bennu mission; lineage from the Phoenix SSI/RAC, Mars Pathfinder and Mars Polar Lander SSI, and Cassini/Huygens DISR imagers (57) | ... | Flight-proven mechanism (57) |

**Table 2** *continued on next page*

**Table 2** *(continued)*

| Element | ESC baseline | Flight / suborbital heritage | Ground / laboratory heritage | Demonstrated performance |
|---|---|---|---|---|

**References**—(1) T. Cook et al. 2015; (2) C. B. Mendillo et al. 2020; (3) C. B. Mendillo et al. 2023; (4) E. Serabyn 2016; (5) G. Serabyn et al. 2019; (6) J. Llop-Sayson et al. 2024; (7) K. Van Gorkom et al. 2024; (8) D. Mawet et al. 2010; (9) D. Mawet et al. 2014; (10) R. Landman et al. 2026; (11) E. S. Douglas et al. 2018; (12) S. K. Vlahakis 2022; (13) A. Potier et al. 2023; (14) J. R. Males et al. 2018; (15) J. R. Males et al. 2024; (16) N. Jovanovic et al. 2015; (17) L. A. Poyneer & D. Dillon 2008; (18) B. Macintosh et al. 2014; (19) C. B. Mendillo et al. 2012a; (20) C. B. Mendillo et al. 2015; (21) G. Singh 2015; (22) G. Singh et al. 2015; (23) K. Derby et al. 2025; (24) K. Milani et al. 2025; (25) V. Bailey 2019; (26) J. E. Krist et al. 2023; (27) S. Y. Haffert et al. 2023; (28) S. Y. Haffert et al. 2022; (29) K. Milani et al. 2023; (30) A. Give'on et al. 2007; (31) T. D. Groff et al. 2015; (32) S. Y. Haffert et al. 2026; (33) A. Potier et al. 2022; (34) K. Van Gorkom et al. 2026; (35) S. K. Subramanian et al. 2026; (36) S. Manojkumar et al. 2026; (37) S. F. Redmond et al. 2022b; (38) S. F. Redmond et al. 2022a; (39) K. Miller et al. 2017; (40) L. Pogorelyuk & N. J. Kasdin 2019; (41) S. P. Bos et al. 2021; (42) A. Potier et al. 2020; (43) R. Galicher et al. 2019; (44) R. M. Anche et al. 2023; (45) N. Murakami et al. 2013; (46) J. N. Ashcraft et al. 2024; (47) J. Rosenbluth et al. 2026; (48) N. Cooper et al. 2026; (49) Beuzit 2006; (50) B. Cho et al. 2023; (51) J. P. Gallagher et al. 2024; (52) O. Daigle et al. 2026; (53) O. Guyon et al. 2018; (54) N. Skaf et al. 2024; (55) J. R. Males et al. 2026; (56) E. Douglas & UArizona Space Astrophysics Lab 2026; (57) B. Rizk et al. 2018.

Draft

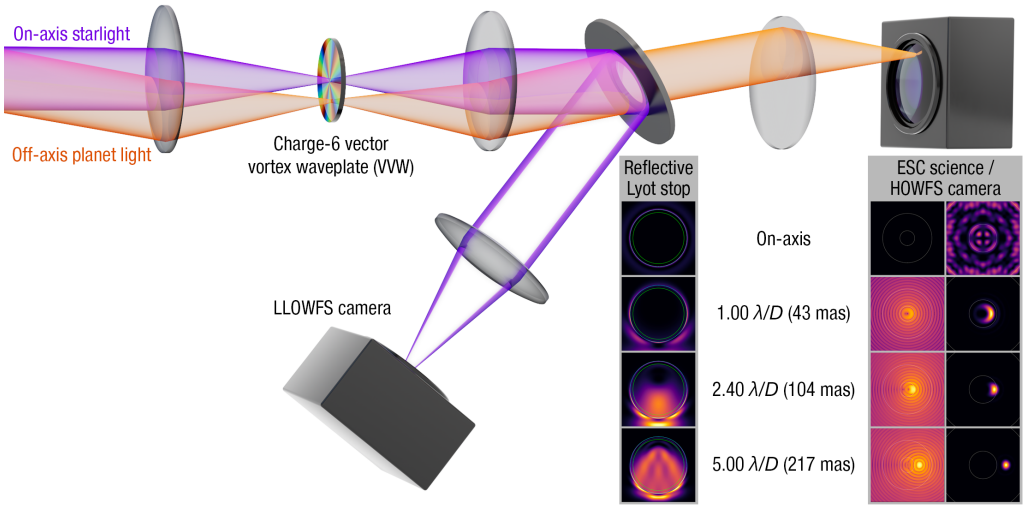



**Figure 1.** Operating principle of the ESC with a VVW and Lyot stop blocking on-axis star light while passing off-axis planet light to the science camera.

### 3.2. *Control loops and block diagram*

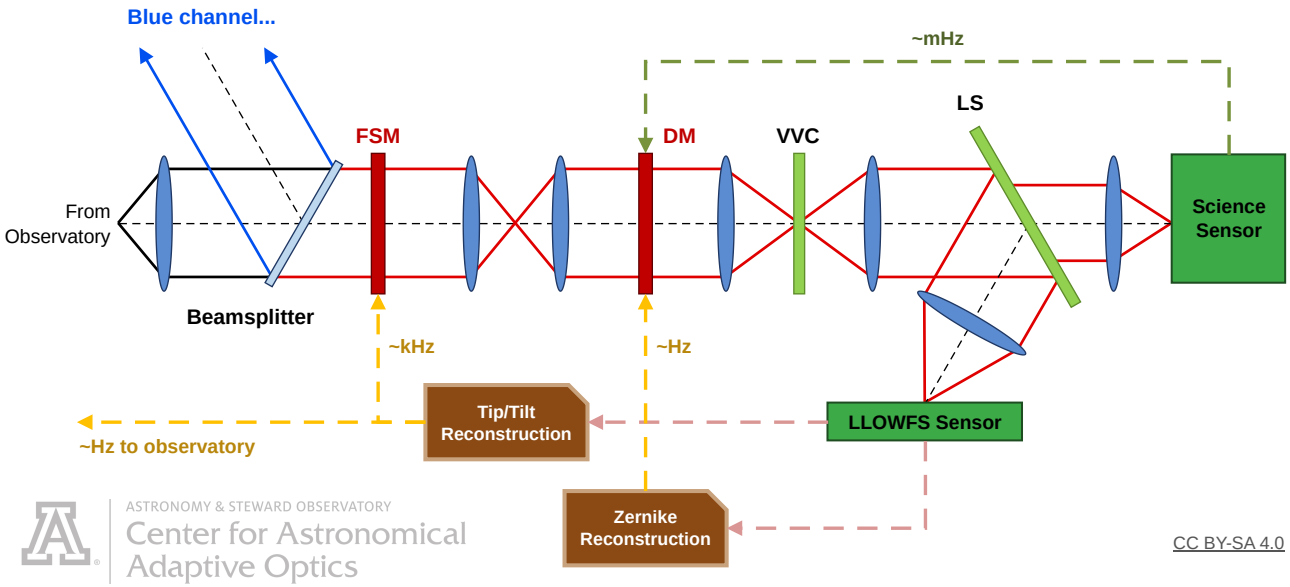



**Figure 2.** ESC wavefront control architecture. Bandwidths are largely photon and read noise limited, with fast steering Mirror (FSM) loop closing a fast point loop with the LLOWFS camera, residual tip/tilt offloads to the telescope and low-order Zernike aberrations are offloaded more slowly to the DM, and photon starved dark-zone maintenance updates applied to the DM much more slowly, at sub-Hertz bandwidths.

#### 3.2.1. *Wavefront control*

The goal of coronagraphy is detection of non-stellar sources at small angular separation $x$ from a star (Figure 1). Raw contrast, $C$, the ratio of the planet photons $\eta_p(x_0, \lambda)$ to starlight in the coronagraph focal plane (G. Ruane et al. 2018b), depends on both the suppression of starlight and the transmission of planet light as a function of separation. Minimization of starlight in a coronagraph depends on effectively nulling the star through interference. An ideal coronagraph removes the stellar plane-wave but slight deviations from a plane wave arising from stellar size, platform

pointing error, or optical aberrations or reflectivity variations manifest as small errors in the stellar electric field, $\alpha$, and are transmitted by the ideal coronagraph. This intensity leakage appears as planet-like "speckles" which non-linearly contribute a background intensity in the final focal plane $\propto \alpha^2$. Optimization of coronagraph "robustness" to errors and active speckle suppression have together been an area of active research for several decades.

We separate the wavefront sensing into two domains: high-order wavefront sensing (HOWFS) measures the starlight that leaks through the coronagraph into the dark zone, while low-order wavefront sensing (LOWFS) measures the low spatial frequencies that do not fall within it.

Many starlight suppression technologies have been developed and several have reached high performance (B. Mennesson et al. 2024), notably starshades, Lyot/Hybrid-Lyot coronagraphs, and VVC. Despite their predicted advantages in normalized intensity and throughput, starshades were not considered for this study due to additional cost and complexity of launching two spacecraft. The next highest-contrast coronagraph technologies, measured by normalized intensity, Lyot and Hybrid Lyot coronagraphs, are highly sensitive to telescope aberrations, both dynamic and polarization (B. S. Gaudi et al. 2020). The vector vortex coronagraph has the advantage of readily being able to trade sensitivity to low-order aberrations against Inner Working Angle (IWA) as a function of topological charge. The phase ramp is set by the topological charge $\ell$ (Equation (1)). Other key coronagraph parameters include: A) maximum throughput of planet light versus starlight, B) IWA, classically defined as the angular separation from the occulted star where coronagraph transmission allows planet brightness to half or more of the maximum planet brightness; C) the Outer Working Angle (OWA) or the maximum angle from the star the coronagraph system effectively suppresses speckles.

Normalized intensity is the focal-plane intensity divided by the peak of the unocculted stellar point spread function (PSF); contrast additionally divides by the off-axis (planet) throughput at that separation (G. Ruane et al. 2018b; K. Van Gorkom et al. 2025). The vortex mask imparts an azimuthal phase ramp

$$\phi(\theta) = \ell\,\theta, \qquad t(\theta) = e^{i\ell\theta}, \tag{1}$$

where $\ell$ is the topological charge, so the phase wraps by $2\pi\ell$ per revolution about the optical axis. Among vortex coronagraphs, charge-4 vortex LCP coronagraphs have reached the highest laboratory contrast (B. Mennesson et al. 2024), but have over an order-of-magnitude greater leakage for equivalent telescope pointing and low-order aberrations versus charge-6 vortex coronagraphs (e.g., G. Ruane et al. 2018a). This robustness to aberrations comes at the trade-off of a larger theoretical IWA of $2.4\lambda/D$ vs $1.75\lambda/D$ (D. Mawet et al. 2009; G. Ruane et al. 2018a).

Our planned charge-6 vector vortex waveplate design has reached $\lesssim 10^{-8}$ contrast on the SCoOB testbed (K. Van Gorkom et al. 2024, see also Figure 7).

We present the design (Figure 3) in order of interaction with exoplanet information rather than importance.

### 3.3. *Dichroic beamsplitter*

The red and blue arms of the coronagraph are split by a dichroic beamsplitter optimized to minimize wavefront error in each arm (J. Rosenbluth et al. 2026). Internal to each coronagraph arm, fine pointing errors not corrected by M4 and the context camera guiding loop will be corrected by an FSM. The FSM controls the fine wavefront tilt using rejected light from the coronagraph further downstream.

The subsequently stabilized on-axis beam will pass through a relay mirror configuration creating a conjugate plane to the system stop M1, where the MEMS deformable mirror (DM) resides.

### 3.4. *Fine pointing*

The FSM centers the target star on the vortex mask. A similar system flew on the PICTURE and PICTURE-B sounding rockets and demonstrated 5 mas pointing control on a 0.5 m telescope (C. B. Mendillo et al. 2012a; E. S. Douglas et al. 2018). The same Physik Instrumente piezoelectric stage (S-316) is planned. Similar PZT-based fine-steering systems have also been used on-orbit (J.-P. Wuelser et al. 2004).

### 3.5. *Polarization filtering*

A linear polarizer followed by a quarter wave plate (QWP) circularizes light into the VVC and a downstream QWP and linear polarizer reject non-circularized light. This single incident circular polarization state improves broadband VVC contrast (N. Murakami et al. 2013) and will provide polarimetric information when the observatory is rolled.

Draft

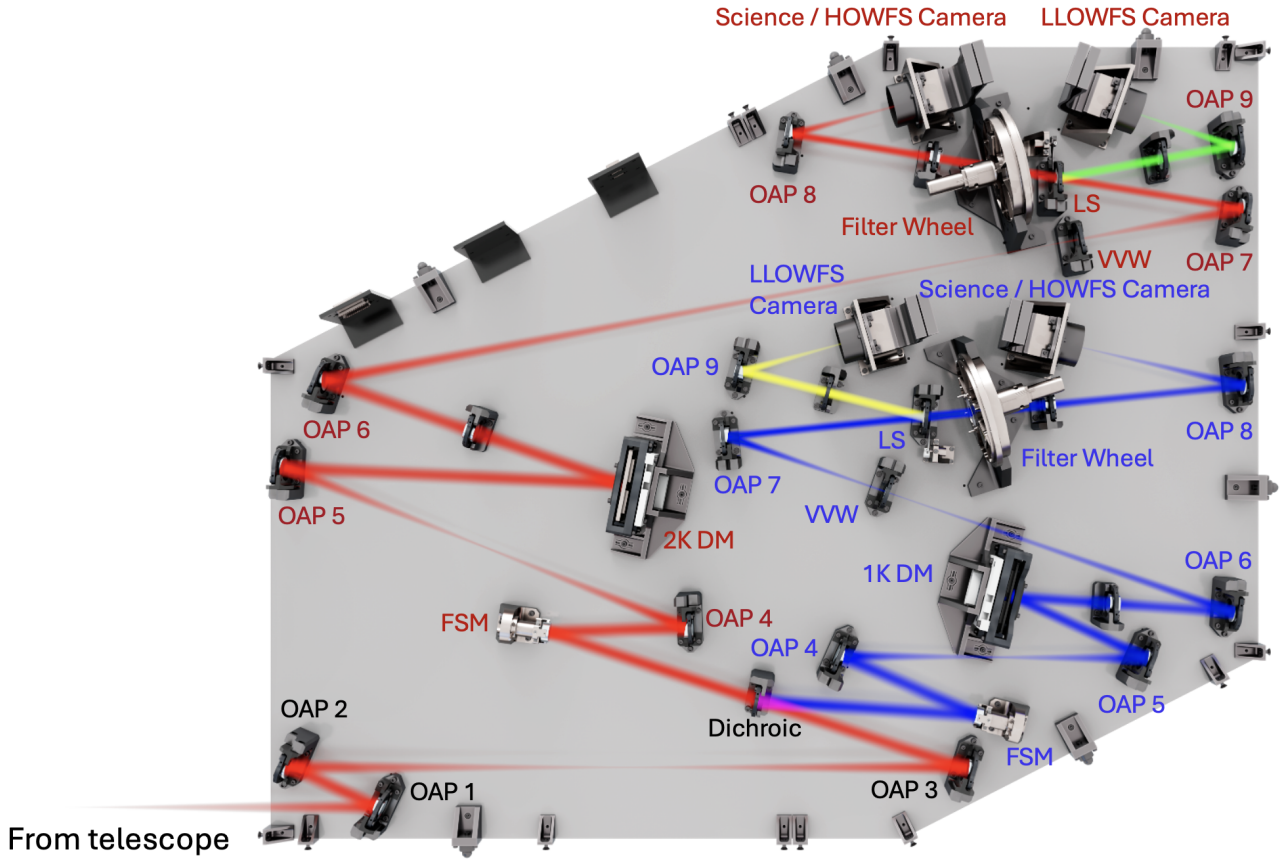



**Figure 3.** Rendering of the two arms of the ESC. Diverging light enters from the telescope focal plane and is split at the dichroic beamsplitter into two independent channels; the science/HOWFS paths are shown in red and blue and the LLOWFS pick-offs in green and yellow, respectively. The f-ratio of the beam at the VVW is conserved and the pupil is matched to each DM, so the blue channel with the Kilo-C DM has the smaller footprint. Besides wavelength, the primary difference between the arms is the number of DM actuators; the red channel with the 2K DM maximizes the outer working angle and achievable contrast.

### 3.6. *Deformable mirrors*

The red coronagraph channel utilizes a 2K MEMS deformable mirror with 2040 total actuators and 45 illuminated actuators across the aperture.

The blue coronagraph channel utilizes a Kilo-C-1.5 MEMS deformable mirror with 952 total actuators and 30 illuminated actuators across the aperture.

The 1K class MEMS DMs (34 actuators across the full array, 30 illuminated), the Boston Micromachines Kilo DM, has extensive heritage of operational testing (see Table 2). BMC Kilo-DMs have been operated on a sounding rocket flight (E. S. Douglas et al. 2018), vibration and thermal cycled and tested for coronagraphy (C. M. Prada et al. 2021), tested for cryogenic space operation by JAXA (A. Takahashi et al. 2017) and are widely used in high-contrast testbeds with electric-field conjugation (EFC), including the Caltech HCST (N. Jovanovic et al. 2018) and the STScI HiCAT (M. N'Diaye et al. 2013), vacuum coronagraphic testing for the EXCEDE mission (E. A. Bendek et al. 2014; R. Belikov et al. 2014; D. Sirbu et al. 2015) and for a NASA TDEM on the JPL vacuum surface gauge (P. A. Bierden et al. 2013).

The 2K class mirror (50 actuators across the full array, 45 illuminated) is physically larger and more sensitive to launch loads. A custom chip carrier was previously developed and has been demonstrated at the High-Contrast Imaging Testbed (HCIT) facility at NASA's Jet Propulsion Laboratory for space coronagraph applications (A. Potier et al. 2023).

### 3.7. *Vector vortex waveplate*

The "corrected" complex field from the DM is focused to the VVC using a slow focusing mirror providing a ∼f/45 beam at the center of the phase mask. VVCs have been demonstrated on sky in the infrared (IR) at a variety of observatories (D. Mawet et al. 2014). At visible wavelengths, NASA TDEM studies (E. Serabyn 2016; G. Serabyn et al. 2019) have demonstrated the necessary contrasts ($1.3 \times 10^{-8}$ at 575 nm and 10% bandwidth; G. Serabyn et al. 2019) with a VVC in the laboratory. The LCP VVC mask minimizes flight, or operational, risk because any potential recognized flaws, notably on-axis defects, if present, are identifiable upon manufacture and initial testing, allowing prompt program remediation (G. Serabyn et al. 2019). Comparable LCP VVCs have flown on the PICTURE-C high-altitude balloon (T. Cook et al. 2015; C. B. Mendillo et al. 2020, 2023).

The typical LCP mean index of refraction is 1.6 and to minimize internal reflections Ohara S-BAL35R substrates are used to support the VVW. S-BAL35R is a non-browning radiation resistant glass with an index of refraction of 1.59. Analogous LCP coronagraph devices have also been subjected to $\gamma$ radiation and not suffered measurable degradation ($< 0.1\%$ change in transmission; R. Landman et al. 2026).

The VVC phase-modulated beam propagates to a 5× pupil diameter off-axis parabola (OAP) mirror, capturing the diffracted light field from the on-axis star. The beam is reflected off an OAP which creates a conjugate pupil at the reflective Lyot stop. Off-axis light from science targets passes through the stop while the on-axis star light is reflected towards the LLOWFS.

The post-VVC beam passes through a filter wheel, another linear polarizer and QWP, and ultimately a focal plane is created on the science sensor.

### 3.8. *Filter selection*

The current baseline selection of ESC filters provide a compact series of discrete reflected-light measurements, spanning red albedo-continuum, blue scattering slope, and methane-sensitive wavelength regions (E. Karkoschka 1994; R. E. Lupu et al. 2016; K. L. Cahoy et al. 2010). F400N uses the shortest ESC wavelength and therefore provides the smallest $\lambda/D$ angular scale; it is explicitly intended for Rayleigh-scattering measurements, close-in planet searches, phase curves, and exozodiacal-dust observations. At these wavelengths, giant-planet reflectance slopes and colors are sensitive to temperature, cloud altitude, aerosols, haze, and atmospheric scattering (E. Karkoschka 1994; K. L. Cahoy et al. 2010). The broader F425W and F450W filters improve photon collection and discovery efficiency at the blue end of the ESC range while sampling the broad blue reflectance slope (K. L. Cahoy et al. 2010).

In the red arm, F620N samples the weak methane feature near 619 nm, while F630N and F659W provide neighboring albedo-continuum measurements; F725.9N samples the stronger methane feature near 727 nm (E. Karkoschka 1994). Combining continuum measurements with methane bands of differing strengths provides greater atmospheric-retrieval leverage than measuring a single methane band and reduces sensitivity to noise-driven uncertainty in the inferred continuum (E. Karkoschka 1994; K. L. Cahoy et al. 2010; B. Lacy et al. 2019). After multiple revisions, the current filter set uses wider bands for efficient discovery and narrower bands to measure the continuum and methane-sensitive regions (R. E. Lupu et al. 2016).

The 400–475 nm blue-arm coverage extends blueward of the documented passbands of the Roman Coronagraph Instrument (CGI), providing access to shorter angular scales, while the red-arm wavelengths overlap portions of Roman's filter architecture and complement Roman's redder imaging and slit-prism spectroscopy capabilities (A. Roy et al. 2026; Roman/CGI Science and Engineering Project Teams 2021).

The full filter complement for both arms is listed in Table 3. ESC filters plotted over a sampling of solar system planet albedos and a predicted exoplanet albedo (from K. L. Cahoy et al. 2010) are shown in Figure 4.

### 3.9. *Sensors*

Coronagraph science and wavefront sensing cameras operate in vastly different regimes. The driving requirement of the LLOWFS sensor is low read noise, short exposure times, and low latency. The science camera operates in dim regimes with very high dynamic range, with very low flux rates in the final science dark zone in close spatial and temporal proximity to very bright speckles. This drives the science camera to prioritize high-quantum efficiency, low-read noise, low dark noise, low pixel cross talk, and low persistence. Project schedule also necessitates off the shelf sensor solutions.

The coronagraph instrument will utilize low-noise complementary metal–oxide–semiconductor (CMOS) sensors with $< 2$ $e^-$ read noise and $< 5\,\mu$m pixels. End-to-end coronagraph operation testing presented by K. Van Gorkom et al.

Draft

**Table 3.** ESC filter complement. Names follow the HST convention (F$\lambda$N narrow, F$\lambda$W nominally 10% $\Delta\lambda/\lambda$, F$\lambda$EW 11% or wider). PIL is the pupil-imaging lens.

| Slot | Name | $\lambda_c$ (nm) | $\Delta\lambda/\lambda$ | Purpose and notes |
|---|---|---|---|---|
| *Red arm* | | | | |
| R1 | F620N | 620 | 2% | WFS, albedo, weak $CH_4$ band at 619 nm. Enables broadband HOWFS; well separated from the dichroic. |
| R2 | F630N | 630 | 2% | Primary filter for all modes; albedo continuum. |
| R3 | F659W | 659 | 10% | Albedo continuum. Broadband enables faster discovery, deeper limits, and broader phase-angle coverage when coupled with narrow sensing filters. |
| R4 | F685N | 685 | 2% | WFS, albedo. Enables broadband HOWFS; 1% width under consideration. |
| R5 | F725.9N | 725.9 | 2% | WFS, $CH_4$. Tests for methane in giant-planet atmospheres. |
| R6 | F656N | 656 | 2% | WFS; matches Roman CGI engineering band 2C. |
| R7 | PIL | 630 | 2% | Pupil-imaging lens (baseline). |
| R8 | Dark block | ... | ... | Baseline. |
| *Blue arm* | | | | |
| B1 | F400N | 400 | 2% | Rayleigh scattering; smallest IWA. Probes close to the star for planet discovery, phase curves, and exozodi. |
| B2 | F450N | 450 | 2% | WFS. Enables broadband HOWFS. |
| B3 | F475N | 475 | 2% | WFS primary mode (baseline). |
| B4 | F450W | 450 | 5–10% | Medium-width discovery. Broadband enables faster discovery, deeper limits, and broader phase-angle coverage when coupled with narrow sensing filters. |
| B5 | F425N | 425 | 2% | WFS. Enables broadband HOWFS. |
| B6 | F425W | 425 | 10% | ... |
| B7 | PIL | 450 | 2% | Pupil-imaging lens. |
| B8 | Dark block | ... | ... | ... |

Draft

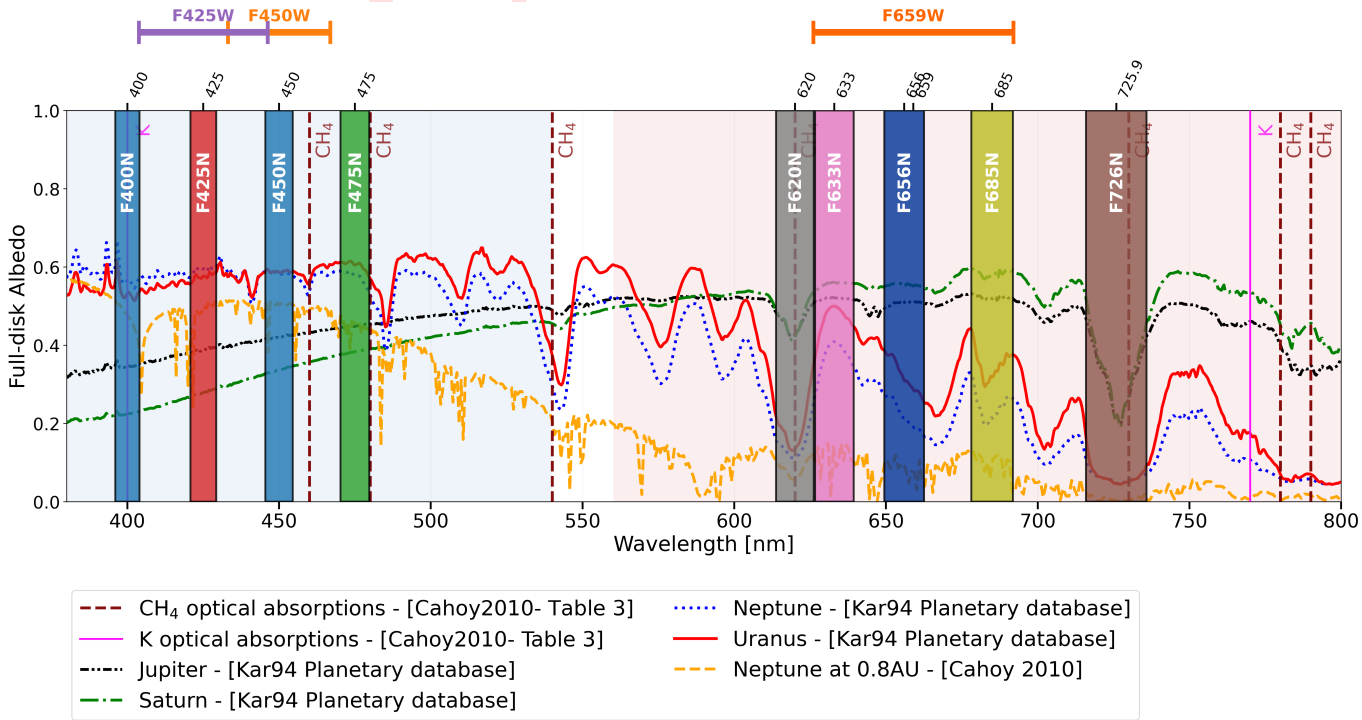



**Figure 4.** Planned ESC science filters plotted with a sampling of measured solar system E. Karkoschka (1994) and modeled giant planet albedos K. L. Cahoy et al. (2010). Narrow-bandwidth "N" filters are shown as vertical shaded bars and wide-bandwidth "W" filters are shown as horizontal bars.

(2024) has shown that sensors with low interpixel bleed (leakage of signal from bright speckles into the dark zone) enable operation without a post-coronagraph field stop. This is key to the compact optical design of the ESC since the image plane relay necessary for a field stop, and possible active alignment elements for positioning of such a field stop, are eliminated. The 0.5 $e^-$ read noise HWK4123 (B. Cho et al. 2023) has been baselined as the LLOWFS sensor. Science sensors requirements include low-interpixel leakage, low read noise, and low dark current. Multiple candidate devices are currently being evaluated, including the IMX492 and the HWK4123. The dark and read noise levels in our regimes make the scientific sensitivity impact of these two sensors is not a major driver; ongoing work to evaluate the interpixel leakage and radiation robustness will drive a future selection.

### 3.10. *Compute and software platform*

To minimize software development time, we chose the established compute and control for adaptive optics (CACAO)+MagAO-X software architecture (O. Guyon et al. 2018; N. Skaf et al. 2024; J. R. Males et al. 2026) which runs on Linux and is graphical processing unit (GPU) accelerated. This software system is optimized for multi-loop wavefront control in a distributed compute system with remote operations. The compute architecture for the ESC is built around SpaceVPX modules based on the NVIDIA Jetson AGX Orin Industrial, with one independently running each ESC arm. Five prototype modules have been launched to the ISS as part of the Neutralino ISS Surveyor payload (**?**).

### 3.11. *High-order wavefront sensing approach*

Using a single DM to control amplitude and phase will produce a one-sided dark zone. In addition to decreasing SWaP using a single DM greatly reduces the size of the control Jacobian, speeding up on-orbit recalibration of the actuator influence functions (H. Zhou et al. 2016).

The baselined image plane wavefront sensing approach is iEFC (S. Y. Haffert et al. 2023), illustrated in Figure 5. Since it is a data-driven empirical wavefront control approach, previous studies have shown that iEFC is robust to misalignments (K. Milani et al. 2023). We have shown the combination of LLOWFS control and iEFC maintained $10^{-8}$ contrast levels in the lab (K. Milani et al. 2025).

Because of the computational flexibility of extreme-wavefront control toolkit (XWCTk) multiple other HOWFS modes are possible. An example optional planned HOWFS mode is the SCC, which relies on a pinhole in the Lyot stop to coherently interfere light with the speckles that are present in the image plane. Planet light will be incoherent with these fringes and unperturbed. SCC wavefront sensing has been demonstrated at THD2 with a MEMS deformable mirror at $10^{-8}$ contrast (A. Potier et al. 2020). Continuous dark-zone maintenance algorithms leverage diversity such as out of field speckles linear dark field control (LDFC) (K. Miller et al. 2017) or small amplitude dithers (L. Pogorelyuk & N. J. Kasdin 2019) to sense and correct for wavefront drifts at frequencies above the spatial control bandwidth of the LOWFS, with little or minimal impact on the collection of science data. Modeling and testing on the SCoOB testbed (S. K. Subramanian et al. 2026) has shown both extended Kalman filtering dark-zone maintenance (DZM) (S. Manojkumar et al. 2026) and LDFC will allow real-time control of speckles in the dark zone; dark-zone maintenance updates are applied to the DM on a notional ∼100 s cadence (the ∼mHz loop in Figure 2).

### 3.12. *Low-order wavefront sensing approach*

Platform jitter and thermal errors are expected to introduce pointing that require fast sensing and control and low-order aberrations that can not easily be sensed in the dark zone. The sensing of these errors via the reflected light from the Lyot Stop (sometimes referred to as the "ring of fire") is accomplished by reimaging with slight defocus, forming a LLOWFS which measures the first 10 Zernike aberrations (tip-tilt through spherical). We have developed and tested simultaneous operation of the LLOWFS correction and iEFC calibration, where a calibrated reference offset corresponding to the currently applied iEFC command is added to the LLOWFS control loop. VVC+LLOWFS has also been demonstrated on sky (G. Singh 2015; G. Singh et al. 2015) and was employed by the PICTURE-C balloon (C. B. Mendillo et al. 2015, 2023).

As a fall-back to iEFC, the instrument will also be capable of image plane wavefront sensing via EFC (A. Give'on et al. 2007; T. D. Groff et al. 2015). EFC uses DM perturbations ("probes") to solve a linear model of the coronagraph system that can be used to iteratively apply DM corrections and suppress residual starlight in the image plane until the desired contrast is reached. EFC works well if wavefront errors are all low-order and no real-time control of the dark zone is required, the mid-to-high spatial frequencies are corrected iteratively over minutes to hours and then

Draft




**Figure 5.** Post-coronagraphic mask speckles (left) before HOWFS and after HOWFS right.

**Table 4.** Comparison of Zemax and Batoid sample statistics.

| Quantity | Zemax | Batoid |
|---|---|---|
| Nominal | 0.0180391 | 0.0179081 |
| Sample size | 6000 | 6000 |
| Minimum sample value | 0.00971277 | 0.0067622 |
| Maximum sample value | 0.0545944 | 0.0437681 |
| Mean | 0.0236643 | 0.0220464 |
| Standard deviation | 0.00637474 | 0.00627267 |
| Variance | $4.06373 \times 10^{-5}$ | $3.93464 \times 10^{-5}$ |
| Sample error | $8.22975 \times 10^{-5}$ | $8.09799 \times 10^{-5}$ |

Draft

the solution is fixed for hours to days of observing time. This "set-and-forget" approach is baselined for the Roman Coronagraph (V. Bailey 2019).

## 4. OPTICAL DESIGN AND ANALYSIS

## 5. DIFFRACTION MODEL: SENSITIVITY ANALYSIS AND INSTRUMENT PERFORMANCE

### 5.0.1. *LLOWFS residuals and DZM*

Testing on the HCIT at JPL has demonstrated vortex coronagraphy at the $\lesssim 10^{-9}$ level (J. Llop-Sayson et al. 2024).

## 6. CONTRAST BUDGET

To calculate the instrumental speckle background ($S_\star$) we sum background terms in a contrast budget, shown in Figure 6 (for derivation of the computed terms see Appendix A). The current best estimate (CBE) total of $7.4 \times 10^{-9}$ is below the allocated total of $1.6 \times 10^{-8}$, consistent with the $10^{-8}$ design goal; the public exposure-time calculator for the ESC[7] adopts $9.7 \times 10^{-9}$, between the CBE and the allocation.

Exposure time calculations include noise from local zodiacal light, detector read and dark noise, disk and stellar leakage ("speckle") photon noise, as well as an additional post-processing corrected speckle noise floor following the formalism developed by B. Nemati et al. (2017, 2020). Assumptions include $5\sigma$ sensitivity per resolution element, as implemented in the public release of the exposure time calculator.

## 7. CONCEPT OF SCIENCE OPERATIONS AND EXPECTED SCIENCE PERFORMANCE

### 7.1. *Concept of operations*

The nominal concept of operations follows a similar procedure to the Roman Coronagraph nominal operational procedure (see J. E. Krist et al. 2023). An observation begins by first acquiring on a bright ($V < 3$) reference star. The initial baseline set of reference stars will utilize the Coronagraph Instrument Reference stars for Exoplanets program (CorGI-REx; J. Hom et al. 2026). The bright reference star, which will be selected to maintain a similar

[7] https://github.com/uasal/stp_etc_esc

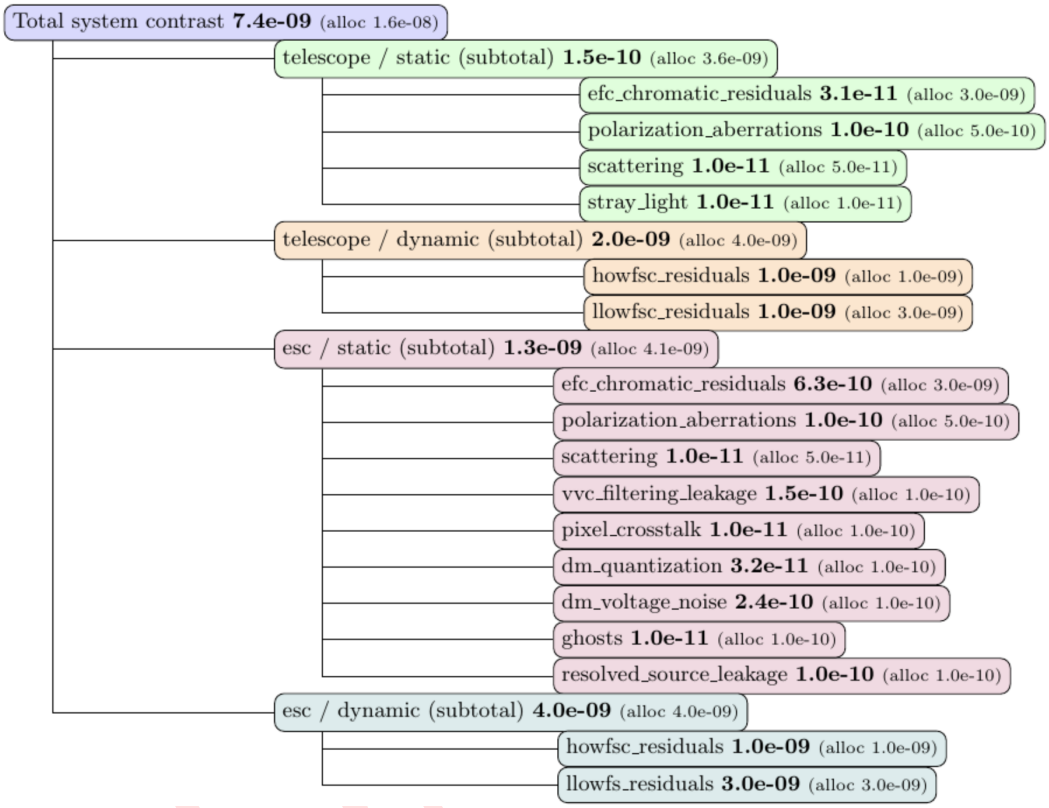



**Figure 6.** Contrast budget to derive $S_\star$ with current best estimate (CBE) in bold and required allocation in parentheses.

pitch angle to the target star, will be used for building response matrices for the high and lower order wavefront loops. Even with ample photons, this operation is time consuming and will be performed on an as-needed basis. With an appropriate calibration in place, dark-zone digging is then initiated using an algorithm such as iEFC (S. Y. Haffert et al. 2023). The ESC aims to utilize its on-board computers to automate as many of the observing steps as possible, including the running of iEFC, and minimize interactions with any ground support. Depending upon the observation, it is possible that three dark zones at ∼120° separations will be derived to ensure a 360° coverage of the target star. Once the dark-zone digging process reaches the desired raw contrast ($\sim 10^{-8}$), a series of science camera images are collected on the reference star to enable reference differential imaging post-processing (RDI).

The precise observing sequence, specifically with regards to when and how the observatory is rolled to enable ADI, is still being explored. Depending upon the observatory's sensitivity to thermal induced variations driven by the changes in pitch and roll angle, as well as the availability of adequate reference stars, the observing strategy may require optimization. An ongoing series of STOP analyses aims to characterize these types of effects and assist in deriving the most efficient strategies, which will then be verified on orbit.

Once observations on the reference star are completed, the observatory will slew to and acquire on the science target of interest, align the star behind the coronagraph focal plane mask, close the loops, and begin taking data. Given the science target is normally fainter than the reference star, longer series of science images are collected (∼2 hours). The dark-zone contrast is maintained by utilizing real-time dark-zone maintenance (see Section 3.11).

Nominally, the observatory then rolls on the target, up to the baselined maximum of 30°. Upon completion, further observations on the reference star may also be performed. As discussed above, the observing sequence is expected to be tailored to the observatory's performance, the target star characteristics, and the science goals.

### 7.2. *Calibration*

The expected calibrations include absolute flux, core throughput, flat fields, astrometry/distortion, dark current, and photometry on the reference and science stars. A similar procedure as described by R. T. Zellem et al. (2022) is

expected, with minor adjustments to calibrations such as flat fields to account for not being able to remove the focal plane mask from the optical path.

### 7.3. *Brief overview of potential science cases*

#### 7.3.1. *Exoplanets*

With the currently described contrast budget and possible ranges on post-processing contrast performance, ESC will be capable of imaging mature Jovian/sub-Jovian analogs in visible reflected light and young Jovian/brown dwarf analogs in self-luminous emission. Filters from 400 to 750 nm were optimized for detecting the narrowband absorption feature from $CH_4$ at 727 nm and for broader albedo continuum measurements (K. L. Cahoy et al. 2010). Multiband photometry is expected to constrain the properties of exo-Jovian atmospheres including composition, metallicity, and the properties of clouds. Understanding the properties of both young and mature Jovian analogs is critical for constraining planetary formation and evolution models.

The Roman Coronagraph, launched on 2026 August 30, plans to perform a pilot survey of known radial velocity (RV) planets in reflected light. Successful detections will significantly constrain orbital solutions of these systems with only prior radial velocity and astrometric data. For these systems detected by the Roman Coronagraph, only photometry at 575 nm and possible spectroscopy around 730 nm are likely to be obtained. Once the orbital solutions are well-constrained, ESC can perform focused observations of Roman-detected planet(s) with its blue channel filters, further bolstering atmospheric characterization efforts.

*Gaia* Data Release 4, scheduled for 2026 December, may also expand the sample of astrometric planet candidates around nearby stars. If these stars are brighter than $V = 5$, ESC would be able to efficiently search for these planet candidates at multiple epochs to account for any nondetections due to suboptimal planet phase at the time of observation.

Draft

#### 7.3.2. *Circumstellar dust*

Circumstellar dust is ubiquitous in planetary systems, with several bright exo-Kuiper belt analogs imaged at optical/near-IR wavelengths. While we do not expect to detect a large number of new extremely bright exo-Kuiper belt analogs, we do expect to detect fainter asteroid belt analogs in the form of rings (similar to our own asteroid belt) and continuous, transport-dominated disks (e.g., Vega; K. Y. L. Su et al. 2024). The morphologies of these systems play a key role in understanding the formation and evolution of planetary system architectures and the possible presence of unseen planetary companions gravitationally perturbing (sub)micron-sized dust grains.

Also likely to be present around many stars is exozodiacal dust. E. S. Douglas et al. (2022) found that the Roman Coronagraph could measure or place upper limits on the surface brightnesses of exozodiacal dust in the outer habitable zones of 74 nearby stars but could only access the inner habitable zones of six stars. With its smaller effective IWA (130 mas at 630 nm), ESC would be able to access at least 10 additional systems. The characterization of exozodiacal dust from a large sample of systems is critical for understanding trends and for ultimately understanding the impact of exozodiacal dust on the detection and characterization of exo-Earths in future high-contrast imaging missions.

#### 7.3.3. *Surveying our nearest stellar neighbors*

Given the relatively high system throughput, ESC would be capable of surveying nearby bright systems ($V < 5$) with high efficiency. A survey of the roughly 230 stars brighter than $V = 5$ would be a deep legacy dataset for optimal planning of future observations at even higher contrast with upcoming and planned instrumentation (e.g., the Habitable Worlds Observatory, HWO). While we do not expect to discover new exoplanets with no prior evidence of radial velocity or astrometric signal, we may serendipitously discover new substellar companions and extended dust disks. A large survey with and without detections of planets and/or dust will constrain theories of planetary system formation, evolution, and architecture. The combination of the large survey of nearby stars and the focused observations of stars with already-known exoplanets will open a new regime of exoplanet direct imaging to systems more analogous to our own solar system. Finally, a large survey of nearby stars, much of which overlaps with the NASA Exoplanet Exploration Program (ExEP) target list for HWO (E. Mamajek & K. Stapelfeldt 2024) will be an impactful precursor investigation for optimizing future high-contrast imaging missions to detect and characterize exo-Earths.

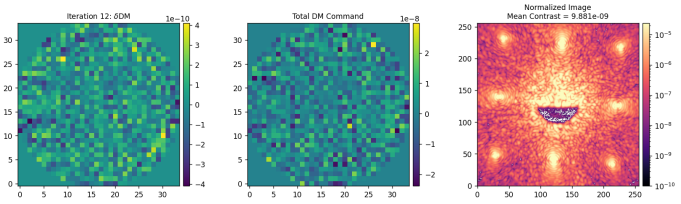



**Figure 7.** Laboratory measurement from the SCoOB testbed recored in Nov 2026 of a dark zone on a dimmer than zero-magnitude simulated star reaching $< 1e-8$ dark zone normalized intensity in a 2% filter.

## 8. CURRENT PERFORMANCE IN THE LAB USING VVC

### 8.1. *Low-flux dark zone*

### 8.2. *Demonstration of LLOWFS*

## 9. SOFTWARE

Our philosophy is to prioritize use of open-source software for design, control, operation, and science data processing. Some of the key software that has contributed to the instrument design includes.

### 9.1. *Flight Software*

We are extending the proven CACAO framework for greater on-orbit autonomy and interfacing with standard spacecraft communication protocols such as Saratoga (L. Wood 2012).

### 9.2. *Simulation*

To simulate ESC performance requires high-fidelty wavefront sensing and control tools. We have developed the Lina Python library K. Milani et al. (2024), which provides a wavefront sensing and control toolbox built on top of GPU accelerated Fraunhofer and Fresnel wavefront in Physical Optics Propagation in Python (POPPY) M. Perrin et al. (2016).

### 9.3. *Systems Engineering*

Automation of systems engineering by extending the Doorstop library J. Browning & R. Adams (2014), and performance budgets with the Budgie tool s. Rinaldi et al. (2026).

## 10. SUMMARY AND DISCUSSIONS

The Lazuli ESC is designed to enable breakthrough high-contrast science in a short timeline, maximizing use of COTS hardware, proven software, and laboratory demonstrated techniques with minimal rework.

Future instrument studies will define the performance of the ESC blue arm, evaluate the wavefront correction performance relative to the Lazuli telescope and the corresponding post-processing factor $f_{pp}$, finalize the detector selection and test the integrated design.

## 11. SOFTWARE AND THIRD-PARTY DATA REPOSITORY CITATIONS

## ACKNOWLEDGMENTS

## AUTHOR CONTRIBUTIONS

AI acknowledgment: large-language model (LLM) tools, including Claude Opus 5.x and Claude Fable 5.x were used in the typesetting, copyediting, agentic coding, and figure generation of this manuscript.

*Facilities:*

*Software:* astropy ( Astropy Collaboration et al. 2013, 2018, 2022), numpy (C. R. Harris et al. 2020), scipy (P. Virtanen et al. 2020), matplotlib (J. D. Hunter 2007), synphot ( STScI Development Team 2018), batoid (J. Meyers

Draft

et al. 2019), POPPY (M. Perrin et al. 2016), lina (K. Milani et al. 2024), CACAO (O. Guyon et al. 2018), XWCTk (J. R. Males et al. 2026), mxlib (J. R. Males 2017), stp_etc_esc (A. Goldtooth et al. 2025)

# APPENDIX

## A. POST-PROCESSING FACTOR AND CONTRAST BUDGET TERMS

Overcoming the systematic error of stellar speckles depends on the underlying speckle distribution which introduces significant uncertainty in the post-processing gain factor, $f_{pp}$. Algorithms to removing speckles depend on diversity and speckle lifetime. Speckle subtraction based on projection of data against a basis set captures temporally stable or "quasistatic" speckles (R. Soummer et al. 2012; A. Amara & S. P. Quanz 2012) while on the other extreme truly random fast-changing speckles average away with each additional measurement.

Following B. Nemati et al. (2017), the post-processing factor $f_{pp}$ is the ratio of the systematic residual left after speckle subtraction to the total speckle signal, $f_{pp} \equiv \sigma_{\rm sys}/(r_{\rm sp}\, t)$, where $\sigma_{\rm sys}$ is the standard deviation of the post-subtraction speckle residual on the scale of a resolution element and $r_{\rm sp}\, t$ is the mean speckle count in the same area over the integration time $t$. The exposure-time calculator adopts $f_{pp} = 0.1$. In the speckle-lifetime calculation of Figure 8, $f_{pp} = \sigma_{\rm sys}/\sigma_{\rm raw}$ with $\sigma_{\rm raw}$ the temporal standard deviation of the unsubtracted speckle intensity; the two definitions coincide for fully modulated speckles, whose temporal standard deviation equals their mean intensity, which is the normalization assumed there. Unlike the $\tau \gg t$ parameterization of B. Nemati et al. (2017), in which $\sigma_{\rm sys}$ grows in proportion to the integration time, panel (d) of Figure 8 also includes the averaging down of residuals whose lifetimes are shorter than the observation.

Draft

# REFERENCES


Amara, A., & Quanz, S. P. 2012, Monthly Notices of the Royal Astronomical Society, 427, 948, doi: 10.1111/j.1365-2966.2012.21918.x

Anche, R. M., Douglas, E., Milani, K., et al. 2023, PASP, 135, 125001, doi: 10.1088/1538-3873/ad0a72

Anche, R. M., Van Gorkom, K. J., Ashcraft, J. N., et al. 2024, The Space Coronagraph Optical Bench (SCoOB): 5. End-to-End Simulations of Polarization Aberrations, arXiv. https://arxiv.org/abs/2406.18886

Anche, R. M., Van Gorkom, K., Milani, K., et al. 2025, in Techniques and Instrumentation for Detection of Exoplanets XII, Vol. 13627 (SPIE), 652–658

Ashcraft, J. N., Douglas, E. S., Anche, R. M., et al. 2024, in Space Telescopes and Instrumentation 2024: Optical, Infrared, and Millimeter Wave, Vol. 13092, 130926K, doi: 10.1117/12.3019204

Ashcraft, J. N., Choi, H., Douglas, E. S., et al. 2022, in Proc SPIE, Proc (arXiv), doi: 10.48550/arXiv.2208.01156

Astropy Collaboration, Robitaille, T. P., Tollerud, E. J., et al. 2013, Astronomy & Astrophysics, 558, A33, doi: 10.1051/0004-6361/201322068

Astropy Collaboration, Price-Whelan, A. M., Sipőcz, B. M., et al. 2018, The Astronomical Journal, 156, 123, doi: 10.3847/1538-3881/aabc4f

Astropy Collaboration, Price-Whelan, A. M., Lim, P. L., et al. 2022, The Astrophysical Journal, 935, 167, doi: 10.3847/1538-4357/ac7c74

Bailey, V. 2019,

Belikov, R., Lozi, J., Pluzhnik, E., et al. 2014, in Space Telescopes and Instrumentation 2014: Optical, Infrared, and Millimeter Wave, Vol. 9143 (International Society for Optics and Photonics), 914323, doi: 10.1117/12.2057028

Bendek, E. A., Belikov, R., Lozi, J., et al. 2014, in Space Telescopes and Instrumentation 2014: Optical, Infrared, and Millimeter Wave, Vol. 9143 (International Society for Optics and Photonics), 91435D, doi: 10.1117/12.2057016

Bendek, E. A., Belikov, R., Lozi, J., et al. 2015, in SPIE Optical Engineering+ Applications (International Society for Optics and Photonics), 960516–960516

Beuzit. 2006, The ESO Messenger, 125, 2

Bierden, P. A., Bifano, T. G., Cornelissen, S., Kasdin, J., & Levine, M. 2013, TECHNOLOGY DEVELOPMENT FOR EXOPLANET MISSONS Technology Milestone White Paper MEMS Deformable Mirror Technology, Document D - 81373, White Paper JPL Document D - 81373, JPL TDEM Whitepaper

Bos, S. P., Miller, K. L., Lozi, J., et al. 2021, Astronomy & Astrophysics, 653, A42, doi: 10.1051/0004-6361/202040134

Bowler, B. P. 2016, PASP, 128, 102001, doi: 10.1088/1538-3873/128/968/102001

Browning, J., & Adams, R. 2014, Journal of Software Engineering and Applications, 07, 187, doi: 10.4236/jsea.2014.73020

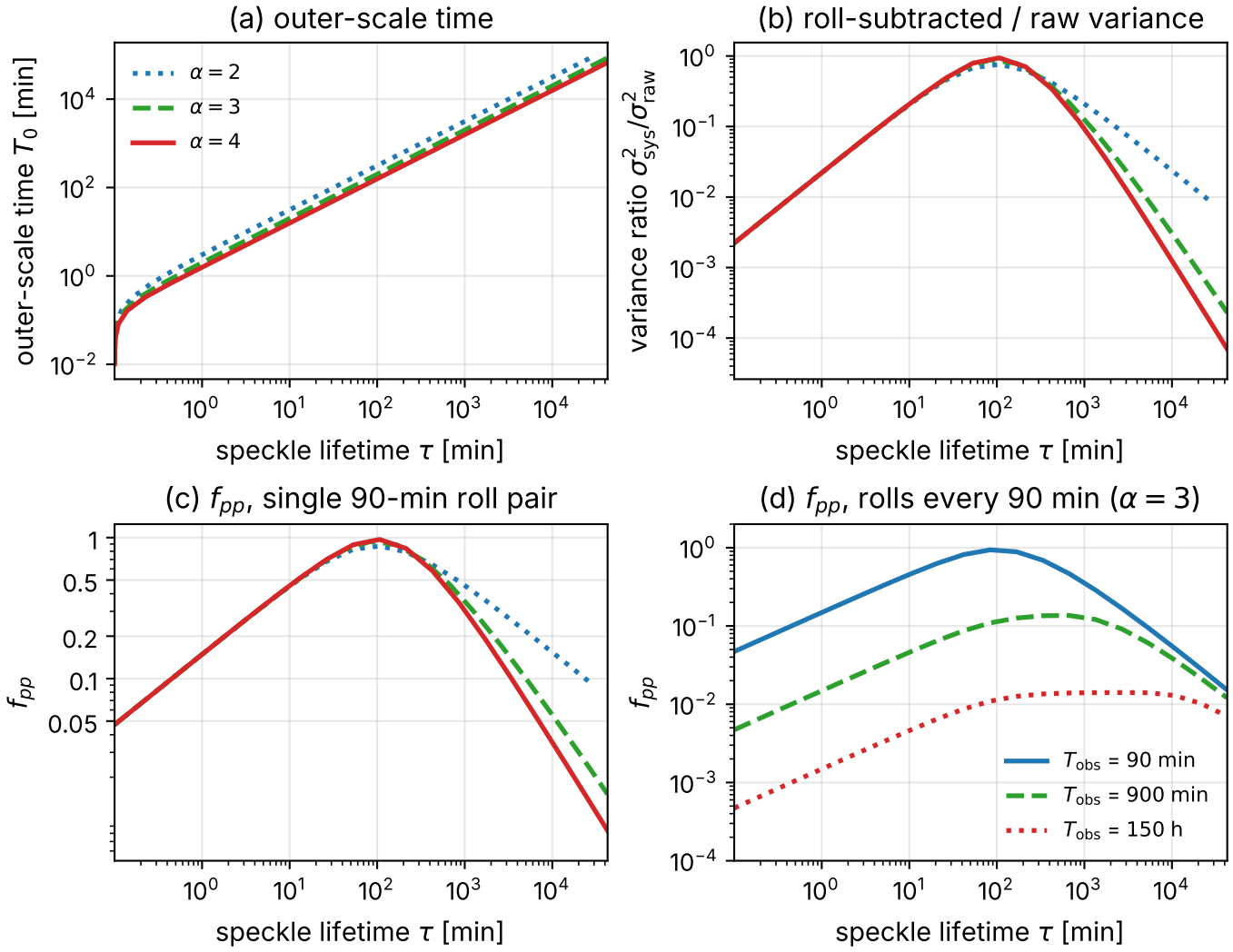



**Figure 8.** Noiseless speckle suppression by 90-minute roll differencing (angular-differential imaging (ADI)) versus effective speckle lifetime $\tau$, for von Kármán exponents $\alpha = 2$ (dotted), 3 (dashed), and 4 (solid). (a) Knee frequency timescale $T_0$ corresponding to each $\tau$. (b) Ratio of the residual variance $\sigma^2_{\rm sys}$ after differencing two 90-minute roll states to the raw speckle variance $\sigma^2_{\rm raw}$. (c) The corresponding post-processing factor $f_{pp} = \sigma_{\rm sys}/\sigma_{\rm raw}$ for a single roll pair; suppression is weakest, $f_{pp} \approx 1$, for lifetimes near the roll cadence, and static speckles cancel as $\Delta/\tau$. (d) $f_{pp}$ for $\alpha = 3$ after averaging the roll-differenced blocks over total observation times of 90 minutes, 900 minutes, and 150 hours. This simulation neglects noise and potential gains from reference star observations and speckle reconstruction from the LOWFS. Future work to characterize the observatory stability will set the post-processing factor $f_{pp}$, which will also be a function of the speckle brightness relative to detector noise floor; this will be a function of target star magnitude biasing observations to brighter stars.

Cahoy, K. L., Marley, M. S., & Fortney, J. J. 2010, ApJ, 724, 189, doi: 10.1088/0004-637X/724/1/189

Cho, B., Johnson, KB., & Shukri, Z. 2023, in International Image Sensor Workshop (IISS (Int. Image Sensors Society))

Cook, T., Cahoy, K., Chakrabarti, S., et al. 2015, J. Astron. Telesc. Instrum. Syst, 1, 044001, doi: 10.1117/1.JATIS.1.4.044001

Cooper, N., Anche, R., Melby, W., et al. 2026, in Advances in Optical and Mechanical Technologies for Telescopes and Instrumentation VII, Vol. 14154 (SPIE), 141549D, doi: 10.1117/12.3105647

Daigle, O., Beaulieu, É., Mehmet, D., & Hu, H. 2026, in Space Telescopes and Instrumentation 2026: Optical, Infrared, and Millimeter Wave, Vol. 14145 (SPIE), 933, doi: 10.1117/12.3104975

Derby, K., Milani, K., Hathaway, G. C., et al. 2025, in Techniques and Instrumentation for Detection of Exoplanets XII, Vol. 13627 (SPIE), 644–651

Douglas, E., & UArizona Space Astrophysics Lab. 2026, in American Astronomical Society Meeting Abstracts, Vol. 247, 108.02

Douglas, E. S., Mendillo, C. B., Cook, T. A., Cahoy, K. L., & Chakrabarti, S. 2018, Journal of Astronomical Telescopes, Instruments, and Systems, 4, 019003, doi: 10.1117/1.JATIS.4.1.019003

Douglas, E. S., Debes, J., Mennesson, B., et al. 2022, PASP, 134, 024402, doi: 10.1088/1538-3873/ac3f7b

Galicher, R., Baudoz, P., Delorme, J.-R., et al. 2019, Astronomy & Astrophysics, 631, A143, doi: 10.1051/0004-6361/201936282

Gallagher, J. P., Buntic, L., Alexani, E., Bouthsarath, K., & Figer, D. F. 2024, in X-Ray, Optical, and Infrared Detectors for Astronomy XI, Vol. 13103 (SPIE), 325–341, doi: 10.1117/12.3019105

Gaudi, B. S., Seager, S., Mennesson, B., et al. 2020, arXiv:2001.06683 [astro-ph]. https://arxiv.org/abs/2001.06683

Give'on, A., Shaklan, S., & Kern, B. 2007, in In the Spirit of Bernard Lyot: The Direct Detection of Planets and Circumstellar Disks in the 21st Century, Vol. 1, 29

Goldtooth, A., Hom, J., Sabhlok, S., & Johnson, J. 2025, stp_etc_esc: Exposure Time Calculator for the ExtraSolar Coronagraph„ https://github.com/uasal/stp_etc_esc

Groff, T. D., Riggs, A. J. E., Kern, B., & Kasdin, N. J. 2015, JATIS, 2, 011009, doi: 10.1117/1.JATIS.2.1.011009

Guyon, O., Schneider, G., Belikov, R., & Tenerelli, D. J. 2012, in Space Telescopes and Instrumentation 2012: Optical, Infrared, and Millimeter Wave, Vol. 8442 (SPIE), 634, doi: 10.1117/12.927188

Guyon, O., Sevin, A., Gratadour, D., et al. 2018, in Adaptive Optics Systems VI, Vol. 10703 (International Society for Optics and Photonics), 107031E, doi: 10.1117/12.2314315

Haffert, S. Y., Males, J. R., Gorkom, K. V., et al. 2022, in Adaptive Optics Systems VIII, Vol. 12185 (SPIE), 2517–2526, doi: 10.1117/12.2630425

Haffert, S. Y., Males, J. R., Ahn, K., et al. 2023, A&A, 673, A28, doi: 10.1051/0004-6361/202244960

Haffert, S. Y., Liberman, J., Males, J. R., et al. 2026, arXiv e-prints. https://arxiv.org/abs/2607.08146

Harris, C. R., Millman, K. J., van der Walt, S. J., et al. 2020, Nature, 585, 357, doi: 10.1038/s41586-020-2649-2

Hom, J., Wolff, S. G., Clark, C. A., et al. 2026, AJ, 171, 36, doi: 10.3847/1538-3881/ae1d68

Hughes, A. M., Duchene, G., & Matthews, B. 2018, arXiv:1802.04313 [astro-ph]. https://arxiv.org/abs/1802.04313

Hunter, J. D. 2007, Computing In Science & Engineering, 9, 90, doi: 10.1109/MCSE.2007.55

Jovanovic, N., Martinache, F., Guyon, O., et al. 2015, Publications of the Astronomical Society of the Pacific, 127, 890, doi: 10.1086/682989

Jovanovic, N., Ruane, G., Echeverri, D., et al. 2018, in Ground-Based and Airborne Instrumentation for Astronomy VII, Vol. 10702 (International Society for Optics and Photonics), 107024E, doi: 10.1117/12.2314325

Karkoschka, E. 1994, Icarus, 111, 174, doi: 10.1006/icar.1994.1139

Kasdin, N. J., & et al. 2020, in Proc SPIE, Vol. 11443, 11443–194

Krist, J. E., Steeves, J. B., Dube, B. D., et al. 2023, JATIS, 9, 045002, doi: 10.1117/1.JATIS.9.4.045002

Lacy, B., Shlivko, D., & Burrows, A. 2019, AJ, 157, 132, doi: 10.3847/1538-3881/ab0415

Landman, R., Doelman, D., Rietjens, J., et al. 2026, SUPPPPRESS: Prototyping and Testing Liquid-Crystal Vector Vortex Coronagraphs with Reduced Polarization Leakage„ https://arxiv.org/abs/2606.10760v1

Llop-Sayson, J., Ruane, G., Serabyn, E., et al. 2024, in Space Telescopes and Instrumentation 2024: Optical, Infrared, and Millimeter Wave, Vol. 13092, 130921Y, doi: 10.1117/12.3020242

Lupu, R. E., Marley, M. S., Lewis, N., et al. 2016, The Astronomical Journal, 152, 217, doi: 10.3847/0004-6256/152/6/217

Macintosh, B., Graham, J. R., Ingraham, P., et al. 2014, PNAS, 111, 12661, doi: 10.1073/pnas.1304215111

Maier, E. R., Douglas, E. S., Kim, D. W., et al. 2020, in Space Telescopes and Instrumentation 2020: Optical, Infrared, and Millimeter Wave, Vol. 11443 (International Society for Optics and Photonics), 114431Y, doi: 10.1117/12.2560878

Males, J. R. 2017, Mxlib: A C++ Library for Astronomical Signal Processing and Wavefront Control„ https://github.com/jaredmales/mxlib

Males, J. R., Close, L. M., Miller, K., et al. 2018, in Adaptive Optics Systems VI, Vol. 10703 (SPIE), 76–89, doi: 10.1117/12.2312992

Males, J. R., Close, L. M., Haffert, S. Y., et al. 2024, in Adaptive Optics Systems IX, Vol. 13097, 1309709, doi: 10.1117/12.3019464

Males, J. R., Long, J. D., Haffert, S. Y., et al. 2026, The eXtreme Wavefront Control Toolkit: High-Contrast Imaging Instrument Control for Ground and Space-Based Coronagraphs, arXiv, doi: 10.48550/arXiv.2608.10156

Mamajek, E., & Stapelfeldt, K. 2024, arXiv e-prints, arXiv:2402.12414, doi: 10.48550/arXiv.2402.12414

Draft

Manojkumar, S., Redmond, S. F., Pogorelyuk, L., et al. 2026, JATIS, 12, 041014, doi: 10.1117/1.JATIS.12.4.041014

Mawet, D., Serabyn, E., Liewer, K., et al. 2010, ApJ, 709, 53, doi: 10.1088/0004-637X/709/1/53

Mawet, D., Trauger, J. T., Serabyn, E., et al. 2009, in Techniques and Instrumentation for Detection of Exoplanets IV, Vol. 7440 (International Society for Optics and Photonics), 74400X, doi: 10.1117/12.826569

Mawet, D., Shelton, C., Wallace, J., et al. 2014, in Space Telescopes and Instrumentation 2014: Optical, Infrared, and Millimeter Wave, Vol. 9143 (International Society for Optics and Photonics), 91432T, doi: 10.1117/12.2057274

Mendillo, C. B., Chakrabarti, S., Cook, T. A., Hicks, B. A., & Lane, B. F. 2012a, Appl. Opt., 51, 7069, doi: 10.1364/AO.51.007069

Mendillo, C. B., Hewawasam, K., Howe, G., et al. 2020, 235, 320.02

Mendillo, C. B., Hewawasam, K., Martel, J., et al. 2023, JATIS, 9, 025005, doi: 10.1117/1.JATIS.9.2.025005

Mendillo, C. B., Hicks, B. A., Cook, T. A., et al. 2012b, in Proc. SPIE, Vol. 8442, doi: 10.1117/12.926408

Mendillo, C. B., Brown, J., Martel, J., et al. 2015, in Techniques and Instrumentation for Detection of Exoplanets VII, Vol. 9605, 960519, doi: 10.1117/12.2188238

Mennesson, B., Gaudi, S., Seager, S., et al. 2016, in Space Telescopes and Instrumentation 2016: Optical, Infrared, and Millimeter Wave, Vol. 9904 (International Society for Optics and Photonics), 99040L, doi: 10.1117/12.2240457

Mennesson, B., Belikov, R., Por, E., et al. 2024, JATIS, 10, 035004, doi: 10.1117/1.JATIS.10.3.035004

Meyers, J., Kirkby, D., & Thomas, D. 2019, Batoid„ Lawrence Livermore National Laboratory (LLNL), Livermore, CA (United States) doi: 10.11578/DC.20200708.1

Milani, K., Derby, K., & Douglas, E. 2024, doi: 10.5281/zenodo.11195112

Milani, K., Douglas, E., Haffert, S., & Van Gorkom, K. 2023, Simulating the Efficacy of the Implicit-Electric-Field-Conjugation Algorithm for the Roman Coronagraph with Noise, arXiv, doi: 10.48550/arXiv.2309.04595

Milani, K., Van Gorkom, K., Mendillo, C. B., et al. 2025, in Techniques and Instrumentation for Detection of Exoplanets XII, Vol. 13627 (SPIE), 623–643

Miller, K., Guyon, O., & Males, J. 2017, JATIS, 3, 049002, doi: 10.1117/1.JATIS.3.4.049002

Morzinski, K. M., Norton, A. P., Evans, J. W., et al. 2012, in SPIE MOEMS-MEMS, 825304–825304

Murakami, N., Hamaguchi, S., Sakamoto, M., et al. 2013, Opt. Express, OE, 21, 7400, doi: 10.1364/OE.21.007400

N'Diaye, M., Choquet, E., Pueyo, L., et al. 2013, in Proc SPIE, Vol. 8864, 88641K–88641K–10, doi: 10.1117/12.2023718

Nemati, B., Krist, J. E., & Mennesson, B. 2017, in Techniques and Instrumentation for Detection of Exoplanets VIII, Vol. 10400 (International Society for Optics and Photonics), 1040007, doi: 10.1117/12.2274396

Nemati, B., Stahl, H. P., Stahl, M. T., Ruane, G. J. J., & Sheldon, L. J. 2020, JATIS, 6, 039002, doi: 10.1117/1.JATIS.6.3.039002

Perrin, M., Long, J., Douglas, E., et al. 2016, POPPY: Physical Optics Propagation in PYthon,

Pogorelyuk, L., & Kasdin, N. J. 2019, ApJ, 873, 95, doi: 10.3847/1538-4357/ab0461

Potier, A., Baudoz, P., Galicher, R., Singh, G., & Boccaletti, A. 2020, A&A, 635, A192, doi: 10.1051/0004-6361/201937015

Potier, A., Mazoyer, J., Wahhaj, Z., et al. 2022, Astronomy & Astrophysics, 665, A136, doi: 10.1051/0004-6361/202244185

Potier, A., Prada, C. M., Ruane, G., et al. 2023, JATIS, 9, 029001, doi: 10.1117/1.JATIS.9.2.029001

Poyneer, L. A., & Dillon, D. 2008, in Proc. SPIE, Vol. 6888, 68880H–68880H–10, doi: 10.1117/12.772754

Prada, C. M., Liu, D., Ruane, G., et al. 2021, in Techniques and Instrumentation for Detection of Exoplanets X, Vol. 11823 (SPIE), 209–221, doi: 10.1117/12.2594263

Pueyo, L. 2018, in Handbook of Exoplanets, ed. H. J. Deeg & J. A. Belmonte (Cham: Springer International Publishing), 1–61, doi: 10.1007/978-3-319-30648-3_10-1

Redmond, S. F., Pogorelyuk, L., Pueyo, L., et al. 2022a, JATIS, 8, 035001, doi: 10.1117/1.JATIS.8.3.035001

Redmond, S. F., Pueyo, L., Pogorelyuk, L., et al. 2022b, in Space Telescopes and Instrumentation 2022: Optical, Infrared, and Millimeter Wave, ed. L. E. Coyle, M. D. Perrin, & S. Matsuura (Montréal, Canada: SPIE), 86, doi: 10.1117/12.2630682

Rinaldi, s., Douglas, E., & Ingraham, P. 2026, doi: 10.5281/zenodo.23913421

Rizk, B., Drouet d'Aubigny, C., Golish, D., et al. 2018, Space Sci Rev, 214, 26, doi: 10.1007/s11214-017-0460-7

Roman/CGI Science and Engineering Project Teams. 2021, Coronagraph Instrument Reference Information,

Rosenbluth, J., Anche, R., Van Gorkom, K., et al. 2026, in Advances in Optical and Mechanical Technologies for Telescopes and Instrumentation VII, Vol. 14154 (SPIE), 141541W, doi: 10.1117/12.3105700

Draft

Roy, A., Feldman, S., Klupar, P., et al. 2026, The Lazuli Space Observatory: Architecture & Capabilities, arXiv, doi: 10.48550/arXiv.2601.02556

Ruane, G., Mawet, D., Mennesson, B., Jewell, J. B., & Shaklan, S. B. 2018a, JATIS, 4, 015004, doi: 10.1117/1.JATIS.4.1.015004

Ruane, G., Riggs, A., Mazoyer, J., et al. 2018b, in Space Telescopes and Instrumentation 2018: Optical, Infrared, and Millimeter Wave, Vol. 10698 (International Society for Optics and Photonics), 106982S, doi: 10.1117/12.2312948

Ruane, G., Riggs, A. J. E., Serabyn, E., et al. 2022, Broadband Vector Vortex Coronagraph Testing at NASA's High Contrast Imaging Testbed Facility, arXiv. https://arxiv.org/abs/2207.13742

Serabyn, E. 2016, Technology Milestone White Paper Vortex Coronagraph Technology,

Serabyn, G., Mawet, D., Ruane, G., Mejia-Prada, C., & Jovanovic, N. 2019, TECHNOLOGY DEVELOPMENT FOR EXOPLANET MISSONS: Technology Milestone White Paper Vortex Coronagraph Technology, TDEM White Paper, JPL TDEM Whitepaper

Singh, G. 2015, PhD thesis, Observatoire de Paris

Singh, G., Lozi, J., Guyon, O., et al. 2015, Publications of the Astronomical Society of the Pacific, 127, 857, doi: 10.1086/682726

Sirbu, D., Thomas, S. J., Belikov, R., et al. 2015, in Techniques and Instrumentation for Detection of Exoplanets VII, Vol. 9605 (International Society for Optics and Photonics), 96050J, doi: 10.1117/12.2188752

Skaf, N., Jensen-Clem, R., Hunter, A., et al. 2024, Real-Time Control and Data Standardization on Various Telescopes and Benches, doi: 10.48550/arXiv.2409.13126

Soummer, R., Pueyo, L., & Larkin, J. 2012, ApJ, 755, L28, doi: 10.1088/2041-8205/755/2/L28

STScI Development Team. 2018, Synphot: Synthetic Photometry Using Astropy„ Astrophysics Source Code Library, record ascl:1811.001 http://ascl.net/1811.001

Su, K. Y. L., Gáspár, A., Rieke, G. H., et al. 2024, ApJ, 977, 277, doi: 10.3847/1538-4357/ad8cde

Subramanian, S. K., Van Gorkom, K., Anche, R. M., et al. 2026, in Space Telescopes and Instrumentation 2026: Optical, Infrared, and Millimeter Wave, Vol. 14145 (SPIE), 141451Y, doi: 10.1117/12.3105600

Takahashi, A., Enya, K., Haze, K., et al. 2017, Appl. Opt., 56, 6694, doi: 10.1364/AO.56.006694

Team, T. L. 2019, arXiv:1912.06219 [astro-ph]. https://arxiv.org/abs/1912.06219

Van Gorkom, K., Douglas, E. S., Ashcraft, J. N., et al. 2022, in Proc SPIE (arXiv), doi: 10.48550/arXiv.2208.01155

Van Gorkom, K., Douglas, E. S., Milani, K., et al. 2024, The Space Coronagraph Optical Bench (SCoOB): 4. Vacuum Performance of a High Contrast Imaging Testbed, arXiv. https://arxiv.org/abs/2406.18885

Van Gorkom, K., Anche, R. M., Mendillo, C. B., et al. 2025, Journal of Astronomical Telescopes, Instruments, and Systems, 11, 042203

Van Gorkom, K., Anche, R. M., Subramanian, S. K., et al. 2026, in Space Telescopes and Instrumentation 2026: Optical, Infrared, and Millimeter Wave, Vol. 14145 (SPIE), 1414567, doi: 10.1117/12.3105631

Virtanen, P., Gommers, R., Oliphant, T. E., et al. 2020, Nature Methods, 17, 261, doi: 10.1038/s41592-019-0686-2

Vlahakis, S. K. 2022,

Wood, L. 2012, in First Annual CCSR Research Symposium (CRS 2011), doi: 10.48550/arXiv.1204.3263

Wuelser, J.-P., Lemen, J. R., Tarbell, T. D., et al. 2004, in Proc SPIE, ed. S. Fineschi & M. A. Gummin, San Diego, California, USA, 111, doi: 10.1117/12.506877

Zellem, R. T., Nemati, B., Gonzalez, G., et al. 2022, Nancy Grace Roman Space Telescope Coronagraph Instrument Observation Calibration Plan, arXiv, doi: 10.48550/arXiv.2202.05923

Zhou, H., Nemati, B., Krist, J., et al. 2016, in Proc SPIE, ed. H. A. MacEwen, G. G. Fazio, M. Lystrup, N. Batalha, N. Siegler, & E. C. Tong, 990419, doi: 10.1117/12.2232211

Zurlo, A. 2026, in Encyclopedia of Astrophysics (First Edition), ed. I. Mandel (Oxford: Elsevier), 395–418, doi: 10.1016/B978-0-443-21439-4.00006-7

Draft